# Theoretical and experimental investigations on Mn doped $Bi_2Se_3$ topological insulator

Ravi Kumar [1,2] Soma Banik [3,2] Shashwati Sen,[4] Shambhu Nath Jha [5] and Dibyendu Bhattacharyya [1,*]

[1]*Atomic and Molecular Physics Division, Bhabha Atomic Research Centre, Mumbai-400 085, India*

[2]*Homi Bhabha National Institute, Anushaktinagar, Mumbai-400 094, India*

[3]*Synchrotrons Utilization Section, Raja Ramanna Centre for Advanced Technology, Indore-452 013, India*

[4]*Technical Physics Division, Bhabha Atomic Research Centre, Mumbai-400 085, India,*

[5]*Beamline Development & Applications Section, Bhabha Atomic Research Centre, Mumbai-400 085, India*

(Received 28 April 2022; accepted 9 November 2022; published 28 November 2022)

Magnetic ion doping in topological insulators (TI's) has emerged to be important both from technological point of view and for experimental verification of exotic fundamental physical concepts. Magnetic ion doping not only opens up the energy gap in surface states of a TI but also changes its bulk band structure significantly. To observe the effect of magnetic ion doping on electronic band structure of TIs density functional theory based *ab initio* electronic structure calculations have been carried out on 2%, 4% and 6% Mn doped $Bi_2Se_3$ system. To validate the results single crystal of undoped and Mn doped $Bi_2Se_3$ have been grown and have been characterized by angle-resolved photoemission spectroscopy (ARPES) measurements with synchrotron radiation. Most of the results viz., band inversion, gapless surface states and reduction in band gap due to Mn doping, as obtained by theoretical calculations have been verified by ARPES measurements. Additionally, ARPES measurements show opening up of the gapless surface states in Mn doped samples. The samples have also been subjected to x-ray absorption spectroscopy measurements comprising of x-ray near edge structure and extended x-ray absorption fine structure measurements using synchrotron radiation which together conclusively show that Mn ions substitute at Bi sites in $Bi_2Se_3$ lattice.

DOI: 10.1103/PhysRevMaterials.6.114201

## I. INTRODUCTION

Topological insulators (TIs) exhibit insulating nature in the bulk but are conducting at the surfaces. These conducting surface states are gapless, and caused by the strong spin orbit coupling and are protected from scattering by the time reversal symmetry (TRS) [1–6]. In semiconductors usually the valance band is made of $p$ orbitals while the conduction band is constituted with $s$ orbitals. However, some interaction such as spin orbit coupling lifts the degeneracy in $p$ orbitals and if the interaction is strong enough $p_{3/2}$ level can attain higher energy than the $s$ level. This leads to band inversion and if the inversion occurs in between two levels which have opposite parity, it will lead the system into a topological insulator phase [1]. Since spin orbit coupling is a relativistic effect, its effect will be prominent in heavier atoms like Bi, Sb, Hg. Numerous compounds based on these atoms like $Bi_2Te_3$, $Sb_2Te_3$, and $Bi_2Se_3$ are found to be three dimensional TI's with simple band structure and relatively large bulk band gap. Among these TI's $Bi_2Se_3$ have some advantage over others because of its relatively larger bulk band gap and single gapless Dirac cone for surface state in the Brillouin zone [3]. These surface states consist of some interesting properties like spin momentum locking (due to strong spin orbit coupling), which results in a quantum spin Hall effect at room temperature and helical edge states without back scattering. The robustness of these surface states make $Bi_2Se_3$ interesting for applications in quantum computation and spintronics devices [7–9].

In the case of magnetic perturbation in TI's, such as application of an external weak magnetic field break the TRS, which causes opening of the energy gap in surface states at Dirac point. The magnetic TI's are expected to realize the emergence of massive Dirac fermions which may lead to development of new devices [10,11] based on spintronics. The topological magnetoelectric effect [10,12] leads to exotic physical phenomena like quantum anomalous Hall effect [13], magnetic monopoles [14] and a Majorana fermion [15]. Ferromagnetism induced in the TI's through doping of transition metal (TM) impurities play the same role as the external magnetic field and several efforts have been given in last few years to create and study the opening up of surface states near the Dirac point by incorporating TM impurities in TI's, including few studies on Mn doping also [16,17]. Doping of magnetic ions in TI's not only opens up the gap in the surface states, but also changes their bulk band structure significantly, thus changing the magnetic and electronic properties of the samples. In a recent communication [18], we have also reported detailed first-principles calculations using density functional theory (DFT) of the bulk band structure of $Bi_2Se_3$ doped with various TM ions. Moreover, there are contradictory reports also on whether this opening up of the gap in surface states in TI's is due to magnetic ion impurities or not, since similar band opening at Dirac point has also been observed by Sánchez-Barriga *et al.* [19] by nonmagnetic impurities also. Hence more theoretical and experimental works are necessary

*Corresponding author: dibyendu@barc.gov.in

 

to confirm that TM impurities can indeed be used to create gap in the surface states of TI's at Dirac point.

In this paper, we investigate the role of Mn doping with different concentration in $Bi_2Se_3$ topological insulator both theoretically and experimentally. We have theoretically investigated the effect of Mn doping at the Bi substitutional site in $Bi_2Se_3$ for 2%, 4%, and 6% Mn concentration using DFT calculations. We have investigated the structural changes in $Bi_2Se_3$ lattice upon Mn doping, stability of Mn doped $Bi_2Se_3$ have been tested by calculating formation energy and effect of doping on electronic bulk band structure of $Bi_2Se_3$ has been investigated. To confirm the findings of theoretical investigations we have grown high quality single crystals of undoped, 2%, 4%, and 6% Mn doped $Bi_2Se_3$. The crystallinity of these samples have been confirmed by x-ray diffraction (XRD) measurements while the effect of doping on electronic bulk and surface band structure have been confirmed by angle resolved photoelectron spectroscopy (ARPES). The local structure of these crystals have further been investigated using x-ray absorption spectroscopy (XAS) technique comprising of both x-ray near edge structure (XANES) and Extended x-ray absorption fine structure (EXAFS) measurements.

## II. COMPUTATIONAL DETAILS

The *ab initio* electronic structure calculations based on DFT was performed using Vienna *Ab initio* Simulation Package (VASP) [20–23], employing plane wave methods and using projector-augmented wave [24,25] pseudopotentials for electron-ion interactions. The generalized gradient approximation of Perdew-Burke-Ernzerhof [26] was adopted to get the exchange and correlation effect. For calculations of the van der Waals forces, we have used DFT + D2 [27] method.

## III. EXPERIMENTAL DETAILS

High quality single crystals of undoped and 2%, 4% and 6% Mn doped $Bi_2Se_3$ were grown by vertical Bridgman technique in a quartz crucible of diameter 10 mm. Before growth, the quartz crucibles were cleaned with 10% HF solution followed by alcohol and were fired at 1000 °C for 10 h to remove all impurities. All elements of high purity (> 99.99%) were taken in desired stoichiometry and loaded in the crucibles and sealed under vacuum of $10^{-5}$ torr. Initially the material was heated to 850 °C and kept at this temperature for 75 h. to ensure proper formation of the $Bi_2Se_3$ phase. After 75 h the furnace was cooled to 800 °C and was maintained at this temperature for next 24 h. Subsequently, the crucible was lowered from the hot zone which was maintained at 800 °C to the cold zone maintained at 650 °C with a translation speed of 0.5 mm/hr. The furnace was then cooled to 550 °C and the crystal was further annealed at 550 °C for 48 h to remove any residual strain in the lattice. The furnace was finally cooled to room temperature to remove the crystal.

The initial structural characterization of these crystals were carried out using x-ray measurements on cleaved crystal surface at room temperature, in a laboratory x-ray diffraction equipment (PROTO HR XRD) using Cu $K_\alpha$ ($\lambda = 1.54$ Å) radiation. The ARPES measurements were done at the ARPES beamline (BL-10) of Indus-2 synchrotron radiation source [28]. To perform the ARPES measurements, the samples were cleaved to obtain atomically clean surface inside the preparation chamber having vacuum $\sim 5.5 \times 10^{-11}$ mbar and were then moved to the measurement chamber. The measurements were done using He $I_\alpha$ lamp ($h\nu = 21.2$ eV) and synchrotron radiation of $h\nu = 83.2$ eV at a temperature of 20 K with energy resolution of 20 and 40 meV, respectively. The ARPES data were recorded in the normal emission mode with respect to the electron energy analyzer (SPECS Phoibos 150) with angular resolution of 0.2 deg. It should be noted that prior to each measurement the ARPES intensity from the sample is maximized by optimizing the alignment of the sample for normal emission. Almost symmetric angular distribution of ARPES data ensures that there is negligible misalignment in the sample. The XAS data of the samples at Bi $L_3$ edge, Se K edge and Mn K edge were collected at the Energy-Scanning EXAFS beamline (BL-9) at the Indus-2 Synchrotron Source (2.5 GeV, 100 mA) at Raja Ramanna Centre for Advanced Technology (RRCAT), Indore, India [29,30]. The Mn doped $Bi_2Se_3$ crystal were mixed thoroughly with cellulose using a mortar pestle in such a way that the absorption edge jump lies around 1 and then pressed the total powder mixture into a pallet of 10 mm diameter. The XAS measurements have been done in transmission mode at Bi $L_3$ edge and Se K edge, and in fluorescence mode for Mn K edge. In transmission mode the incident x-ray beam was allowed to pass through the thin pelletized sample and two ionization chambers, each of 30 cm length were used to detect the incident flux ($I_0$) and photon flux after transmission from the pellet sample ($I_t$). The absorption coefficient $\mu$ was calculated as a function of energy using the relation, $I_t = I_o \exp(-\mu x)$ where $x$ is the thickness of the sample. In fluorescence mode, the sample is placed at 45 ° with the incoming beam, an ionization chamber detector placed prior to the sample and a Si drift detector placed at 90° to the incident beam have been used for measuring the incident flux ($I_0$) and the fluorescence signal ($I_f$), respectively, and the absorbance of the sample ($\mu = \frac{I_f}{I_0}$) is obtained as a function of energy by scanning the monochromator over the specified energy range.

## IV. RESULTS AND DISCUSSION

### A. Computational results

$Bi_2Se_3$ crystal structure belongs to the R3m space group, for which the primitive unit cell contains two Bi atoms and three Se atoms, however for convenience of indexing [31] we have used a conventional hexagonal unit cell which has three basic unit cells. Each basic unit cell is called quintuple layer (QL), which are weakly bound to each other through van der Waals forces [32]. Each QL consists of five atomic planes with Se1–Bi–Se2–Bi–Se1 atomic order as shown in Fig. 1(a). For doped system we have substituted dopant atom at the Bi site as shown in Fig. 1(b). In order to achieve low doping concentration we have formed a $3 \times 3 \times 1$ supercell system, which consists of nine conventional unit cells with 135 atoms. For 2% Mn doped $Bi_2Se_3$ we have replaced one Bi atom with an Mn atom. Similarly, for 4% and 6% case we have replaced two and three Bi atoms with Mn atoms, respectively. The structure relaxation was carried out with spin orbit coupling with van

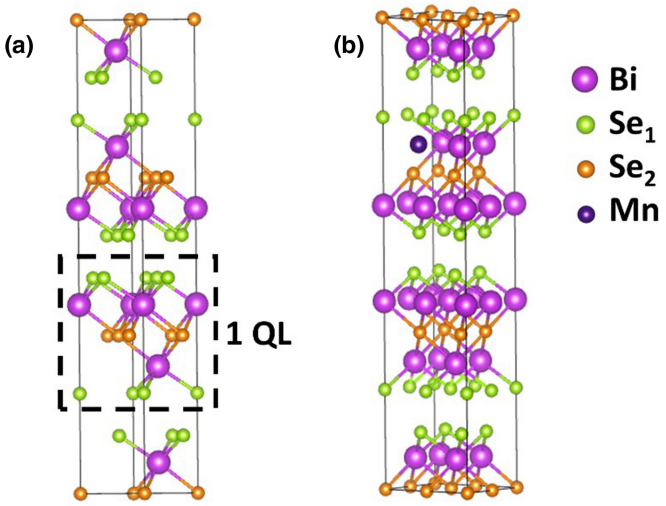


FIG. 1. (a) Crystal structure of $Bi_2Se_3$ hexagonal unit cell. (b) Mn atom doping in $Bi_2Se_3$ at Bi site.

der Waals forces. It should be noted that it is important to consider van der Waals interaction to obtain the relaxed lattice parameters which are in agreement with experimental values. The structure relaxation is terminated when the force acting on each atom were smaller than 0.02 eV/Å. These relaxed structures have been used for final electronic calculations with energy cut-off of 400 eV. The Brillouin zone was sampled by employing a Γ-centered mesh of $2 \times 2 \times 1$ for relaxation of crystal and of $3 \times 3 \times 2$ for total energy calculation. We have also calculated the electronic band structure of surface states for pure $Bi_2Se_3$. To calculate the surface states we have run the calculations on five quintuple layers (∼ 50 Å) thick slab of $Bi_2Se_3$ with a vacuum buffer of 100 Å, so that the top and bottom layer does not interact with each other.

It should be noted here that in case of the 2% Mn doped system, the $3 \times 3 \times 1$ supercell consists of 1 Mn atom only, so for the theoretical calculations we can choose any Bi site since all Bi sites are equivalent. For the 4% doping case we have done seven calculations for different combinations based on the relative positioning of the 2 Mn atoms. The first configuration in which both Mn atoms are in same QL again have three options on the basis of Mn-Mn atom distances. The second configuration in which each Mn atoms are in successive QL's also have three options on the basis of Mn-Mn atomic distances. In the last case (3rd configuration) we have considered both Mn atoms to be in the same Bi atomic plane of a QL. From the theoretical results we can see that there is not much difference among the results for different configurations. In the manuscript we have reported the results for least formation energy configuration which corresponds to both Mn atoms in the same QL. In case of 6% Mn doped system similarly we have considered each of the 3 Mn atoms to be in successive 3 QL's which again corresponds to the lowest energy configuration.

The lattice constant values for Mn doped $Bi_2Se_3$ after structure relaxation are presented in Table I while Table II shows the values for formation energy of 2%, 4% and 6% Mn doped $Bi_2Se_3$. The formation energies were calculated by

TABLE I. The optimized lattice parameters for Mn doped $Bi_2Se_3$.

| Sample name | Lattice parameter (a) Å | Lattice parameter (c) Å |
|---|---|---|
| $Bi_2Se_3$ | 4.13 | 28.69 |
| $Bi_{1.96}Mn_{0.04}Se_3$ | 4.125 | 28.74 |
| $Bi_{1.92}Mn_{0.08}Se_3$ | 4.12 | 28.741 |
| $i_{1.88}Mn_{0.12}Se_3$ | 4.11 | 28.66 |

using the following equation [33]:

$$E_{\text{Form}} = E_{\text{Bi}_{2-x}\text{Mn}_x\text{Se}_3} - E_{\text{Bi}_2\text{Se}_3} + n\mu_{Bi} - n\mu_{Mn}, \qquad (1)$$

where, $E_{\text{Bi}_{2-x}\text{Mn}_x\text{Se}_3}$ and $E_{\text{Bi}_2\text{Se}_3}$ are the total energies of Mn doped and pure $Bi_2Se_3$ and $\mu_{Bi/Mn}$ is the total energy per atom of the respective bulk phase and $n$ is the number of Mn atoms substituted at Bi sites in the supercell.

From Table I it can be seen that the lattice constant $a$ of doped $Bi_2Se_3$ systems are less than that of the pristine system. This is consistent with the theoretical result reported by us [18] for various transition metal doping and observed experimentally by Zhang *et al.* [34] also for Co doped $Bi_2Se_3$ and is expected since ionic radii of TM's are less than that of $Bi^{+3}$. The decrease in lattice constant a causes rise in the total energy of bulk, which has been compensated by increasing the van der Waals gap between the QLs that explains the increment in the lattice constant $c$ with the onset of doping. However, with increase in doping concentration $c$ value again decreases. This is due to the fact that in Mn doped samples, Se atoms move toward Mn atoms and this tries to reduce the size of the QL in the z direction. Thus in Mn doped samples there is a competition between the two phenomena: reduction in QL size and increase in van der Waals gap and for 6% Mn doped sample the former overweighs the later leading to a decrease in lattice parameter $c$.

Table II shows that the formation energies of all Mn doped samples are positive which is consistent with the results reported by us [18] for various TM doped $Bi_2Se_3$ samples for substitution at Bi site. Abdalla *et al.* [35] and Zhang *et al.* [34,36] have also obtained positive formation energies for Mn substitution at Bi sites.

Figure 2(a) shows theoretically simulated bulk electronic band structure of $Bi_2Se_3$, which shows an indirect bulk band gap of 0.28 eV, while the surface states in a 5 QL thick slab of $Bi_2Se_3$ are shown in Fig. 2(b). The phenomenon of band inversion at Γ point which occurs due to strong spin-orbit coupling and manifested by the presence of Bi 6p states at valence band maxima and Se 4p states at conduction band minima is also clearly seen in Fig. 2(a). The simulated electronic bulk band structure of $Bi_2Se_3$ shows an indirect band

TABLE II. Formation energies for Mn doped $Bi_2Se_3$ per unit cell (15 atoms).

| Sample name | Formation energy (eV) |
|---|---|
| $Bi_{1.96}Mn_{0.04}Se_3$ | 0.067309 |
| $Bi_{1.92}Mn_{0.08}Se_3$ | 0.126355 |
| $Bi_{1.88}Mn_{0.12}Se_3$ | 0.200652 |

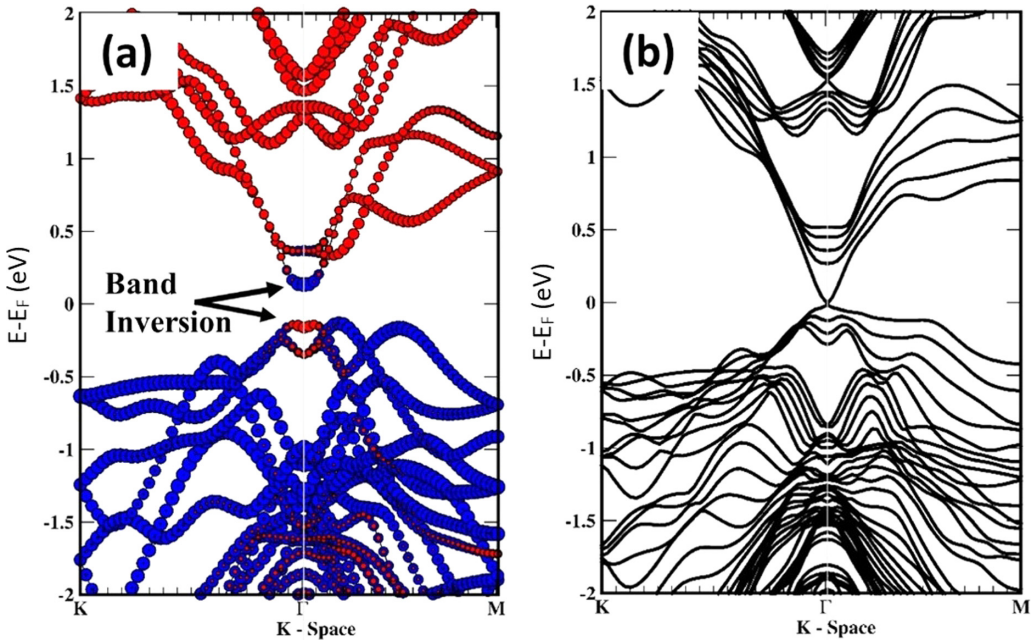


FIG. 2. Theoretically simulated electronic (a) bulk band structure showing the band inversion phenomenon (red circle: Be 6*p* states, blue circle Se 4*p* states) and (b) surface band structure of $Bi_2Se_3$.

gap of 0.28 eV, which is consistent with the ARPES results given in subsequent sections.

Figures 3(a)–3(d) show the electronic band structures and total and partial density of states of undoped and Mn doped $Bi_2Se_3$ systems showing additional states appearing in the bandgap modifying the band structure of pristine $Bi_2Se_3$. It should be noted that, additional bands have appeared in Fig. 3(a) compared to that in Fig. 2(a) which is due to band folding effect. The electronic band structure shown in Fig. 2(a), has been calculated using a conventional hexagonal unit cell of $Bi_2Se_3$, while Fig. 3(a) shows the electronic band structure of a $3 \times 3 \times 1$ supercell of the conventional hexagonal unit cell. As the size increases in real space, the first Brillouin zone in reciprocal space shrinks and hence the normal Brillouin zone gets folded into the supercell Brillouin zone.

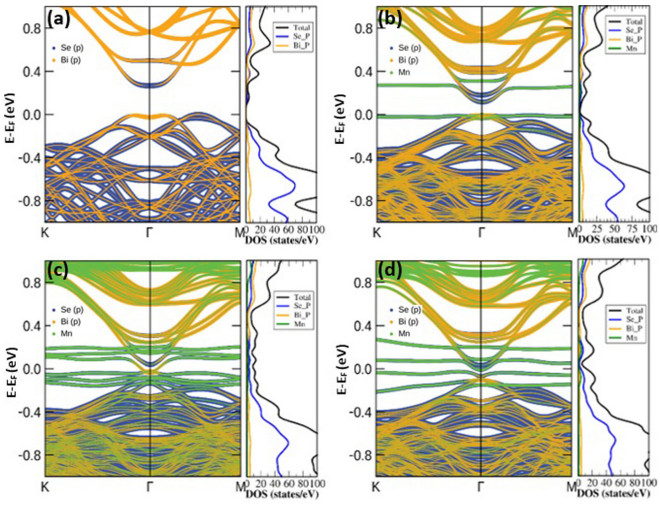


FIG. 3. Electronic band structure, partial and total density of states of (a) $Bi_2Se_3$, (b) $Bi_{1.96}Mn_{0.04}Se_3$, (c) $Bi_{1.92}Mn_{0.08}Se_3$, and (d) $Bi_{1.88}Mn_{0.12}Se_3$. The total DOS, projected Bi-p, Se-p and Mn DOS have been denoted by black, red, green, and blue lines, respectively.

In the case of Mn doped $Bi_2Se_3$, the hybridization between Mn 3d and Se 4p states push the minima of conduction band to the valence band, thus reducing the band gap, the 2% Mn doped $Bi_2Se_3$ shows a bandgap of 0.11 eV. It can also been seen from Fig. 3 that with increase in Mn doping concentration, the Fermi level is pushed inside the valence band making the system p-type, an observation made by other workers also [16]. Other workers have also reported that for doped $Bi_2Se_3$ systems, structural relaxation brings Se atoms significantly closer to the dopants, thus enhancing the hybridization [35,36].

### B. Experimental results

Figure 4 shows the XRD pattern of $Bi_2Se_3$ and Mn doped $Bi_2Se_3$ crystals. These crystals show only (00l) (l = 3n, where n is an integer) type of reflections over $2\theta$ range of 10°–80° without any other peaks indicating that all layers have grown with the c axis parallel to the surface normal and have single phase rhombohedral structure with the space group (*R*3*m*). ARPES data of undoped $Bi_2Se_3$ crystal recorded at $h\nu = 21.2$ eV in Fig. 5(a) shows the bulk bands with band inversion at the valence band maxima. The bulk band shows very good agreement with theoretical calculations [Fig. 2(a)]. Figure 5(a) clearly shows the topological surface state inside the bulk band gap between the conduction and the valence band. We have estimated a bulk band gap of $E_g \approx 0.219 \pm 0.005$ eV from the difference between the valence band edge and the conduction band peak in the energy distribution curve at the Γ point as shown in Fig. 5(d) which is in fair agreement with our theoretical results ($E_g \approx 0.28$ eV).

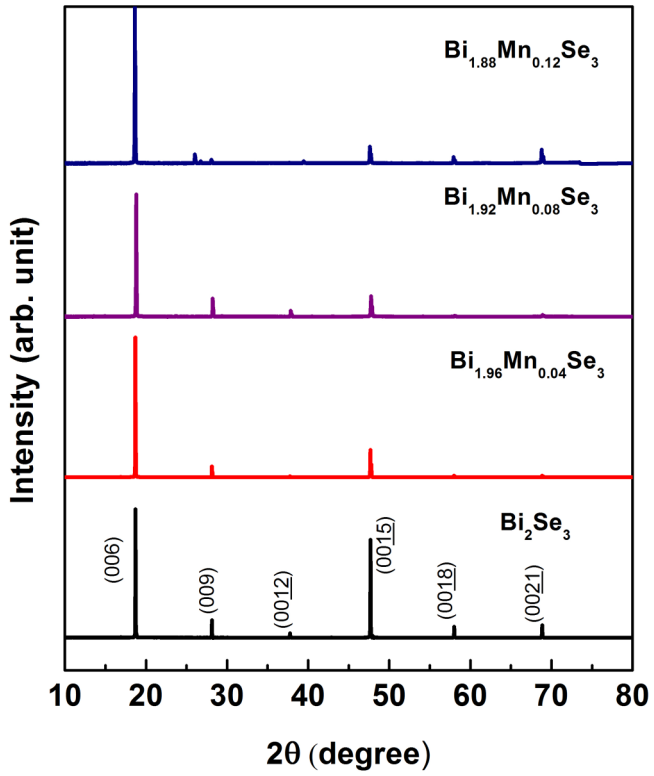


FIG. 4. XRD pattern of $Bi_2Se_3$ and Mn doped $Bi_2Se_3$ crystal.

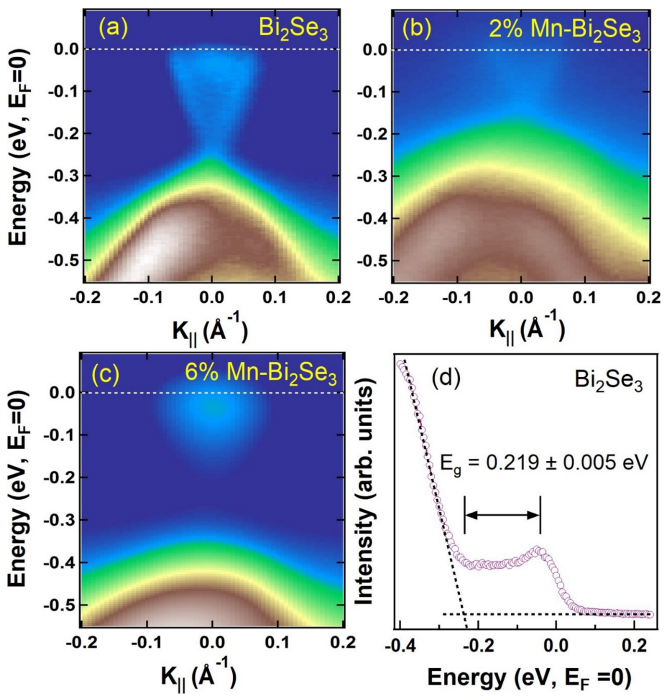


FIG. 5. ARPES data recorded with 21.2 eV photons showing clear topological surface states and energy gap for (a) $Bi_2Se_3$ (b) 2% Mn doped $Bi_2Se_3$, and (c) 6% Mn doped $Bi_2Se_3$. The energy gap between valence and conduction band for the undoped $Bi_2Se_3$ sample has been estimated from the valence band edge and the conduction band peak in energy distribution curves at Γ point in (d). The dashed line is the linear fitting to determine the valence band edge.

It should, however, be mentioned here that $k_z$ dispersion of the bulk conduction and valence band states at the Brillouin zone center are important as shown by various authors and thus ideally the band gap should be estimated by measuring the ARPES data at several photon energies [37,38]. However, our estimate might not be too wrong since Xia *et al.* [4] have observed that for $Bi_2Se_3$ there is no strong $k_z$ dispersion of the lowest lying energy bands (near top of the valence band) which are used to determine the band gap. Kim *et al.* [39] also have compared the single energy ARPES data with theory to find the band gap of $Bi_2Se_3$.

In Figs. 5(b) and 5(c) we have shown the ARPES data recorded with 21.2 eV for 2% Mn and 6% Mn doped $Bi_2Se_3$ samples, respectively. We can clearly see that the valence band edge has shifted towards $E_F$ [Fig. 5(e)] in agreement with the DFT result. The band gap of the 2% Mn doped $Bi_2Se_3$ sample has not been estimated since the conduction band is not clearly observed.

The conduction bands for 6% Mn doped $Bi_2Se_3$ in Fig. 5(c) become quite broad due to increase in disorder in the sample with higher Mn doping and clearly a gap appears in the surface states which is expected due to Mn doping. However, we cannot undoubtedly claim that the opening of the gap in surface state is due to Mn doping only since vanishing of surface states in the experimentally observed electronic structure of Mn doped $Bi_2Se_3$ crystals might also be due to disorders created in the lattice by Mn doping apart from due to magnetic contribution of Mn dopants. We have not tried to find out the band gap of this sample also due to the presence of the gap in the surface state.

It should be noted here that we could not theoretically simulate the surface states near Fermi level for the doped systems since for this we have to take a $3 \times 3 \times 1$ supercell and also 5 QL which increases the number of atoms and thus it increases the computational time significantly.

To understand the contribution of Mn doping in $Bi_2Se_3$, we have also performed the ARPES measurements at $h\nu = 83.2$ eV, with different Bi 6p and Se 4p photoionization cross sections than at $h\nu = 21.2$ eV.

In Fig. 6, the comparison of the bulk bands and surface states recorded with 21.2 and 83.2 eV photon energies are shown for all the samples. If we compare Figs. 6(a) and 6(d) for the pristine $Bi_2Se_3$ sample with the partial density of states plots obtained from DFT calculations (presented in Fig. 3) for the pristine $Bi_2Se_3$ system, it can clearly be seen that the 21.2 eV data in Fig. 6(a) shows that the bands are slightly enhanced in intensity due to the higher photoionization cross section of Se 4p states than that recorded with the 83.2 eV photo energy. Interestingly, the cross-section effect of Se 4p and Bi 6p states at 21.2 eV and 83.2 eV photon energies are more prominently observed in $Bi_2Se_3$ surface states as shown in Figs. 7(a) and 7(b).

We find that there is a shift in the Dirac point from 0.25 eV at $h\nu = 21.2$ eV to 0.4 eV at $h\nu = 83.2$ eV which we believe is due to surface aging of our samples during measurements. There are few other reports also which show shifting of Dirac point during ARPES measurements in $Bi_2Se_3$ samples. Bianchi *et al.* [40] have observed shifting of chemical potential after 3 h in vacuum which causes a shifting of the Dirac point from -0.2 to -0.5 eV. Biswas *et al.* [41] have

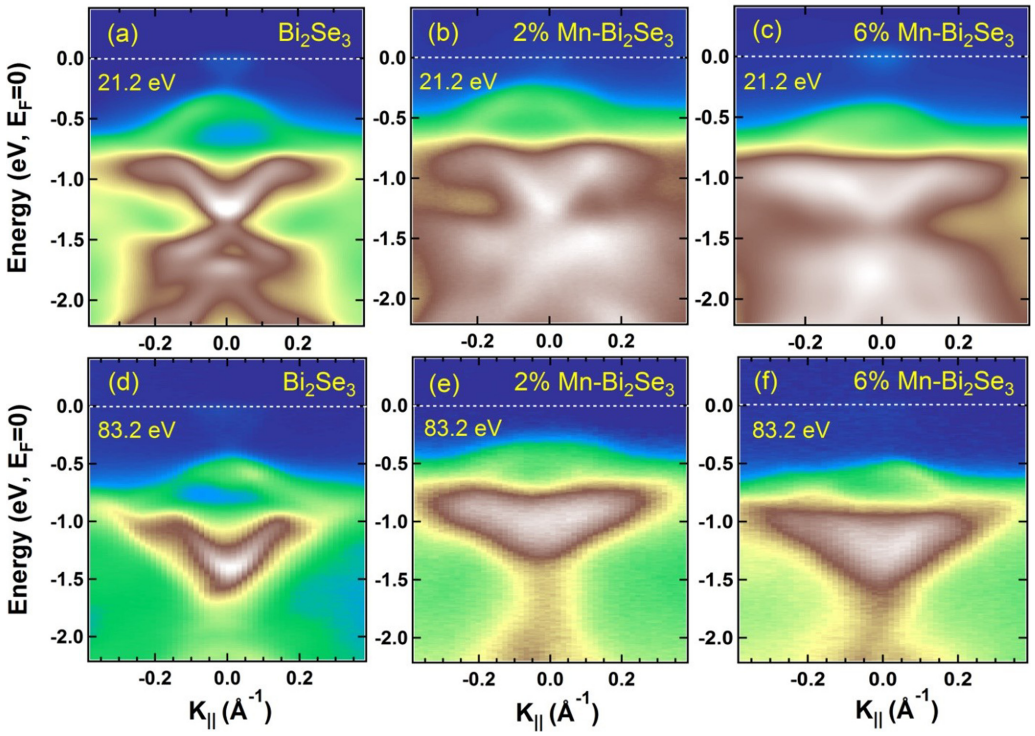


FIG. 6. ARPES data recorded with 21.2 eV photon energy shown for $Bi_2Se_3$ in (a), 2% Mn doped $Bi_2Se_3$ in (b) and 6% Mn doped $Bi_2Se_3$ in (c) while the bands recorded with 83.2 eV photon energy shown for $Bi_2Se_3$ in (d), 2% Mn doped $Bi_2Se_3$ in (e) and 6% Mn doped $Bi_2Se_3$ in (f).

also observed shifting of Dirac point towards higher binding point energy with aging for Se terminated surfaces in $Bi_2Se_3$ due to adsorption of oxygen on sample surface. As has been mentioned in the experimental section of the present manuscript, the ARPES measurements at 21.2 eV photon energy were done using a He I$\alpha$ lamp source while synchrotron radiation was used for measurements with photon energy of 83.2 eV and thus there was a time gap between the two sets of measurements. There is also a very high probability that our samples have Se terminated surfaces during cleaving of $Bi_2Se_3$ crystals, because of weak Van der Waals forces between two quintuple layers.

The effect of Mn doping in $Bi_2Se_3$ leads to structural relaxation which affects both surface states as well as the bulk bands. If we compare Figs. 6(b) and 6(e) for 2% Mn doped $Bi_2Se_3$ and Figs. 6(c) and 6(f) for 6% Mn doped $Bi_2Se_3$ with the electronic band structure with projected atomic orbitals and partial density of states plots obtained from DFT calculations (presented in Fig. 3), it is evident that bulk bands near top of the valence band get broader due to the hybridization between the Se 4p and Bi 6p states with Mn 3d states. The changes in the topological surface states is associated with the hybridization between Se 4p and Mn 3d states. However, it is true that there may be some extra broadening in the experimental band structure data arising from the disorder that might be created in the samples due to Mn doping also.

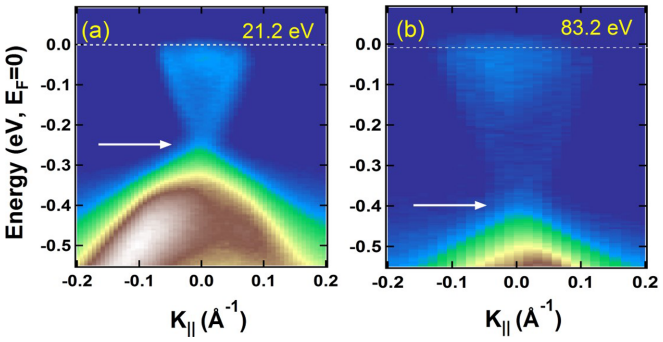


FIG. 7. Topological surface state of $Bi_2Se_3$ collected with (a) 21.2 eV and (b) 83.2 eV. The arrow in the figure shows the position of the Dirac point.

Subsequently we have carried out detail XAS studies on the samples at Bi $L_3$, Se K, and Mn K edges in order to ascertain that Mn doping leads to substitution at the Bi sites only and not at the Se site or interstitial positions. XAS being an element specific tool gives an overall idea of the doped system very effectively, the results are described in the following.

The Bi $L_3$ edge XANES spectra are shown in Fig. 8. It can be seen that the absorption edge of Bi for undoped and Mn doped $Bi_2Se_3$ lie near to that of $Bi_2O_3$, suggesting that Bi is in +3 oxidation state in the sample. However, with increase in doping concentration of Mn the Bi absorption edge is found to shift slightly to lower energy. The shifting of Bi absorption edge to lower energy can be understood in terms of difference in electronegativities of Bi and Mn ions. Mn has less electronegativity compared to Bi ions [42,43], because of which Mn can share its electron for formation of bonds with Se atom more effectively compared to Bi atom. Hence, Bi sites become less positive with higher doping concentration of Mn leading to the shifting of Bi absorption edge to lower energy.

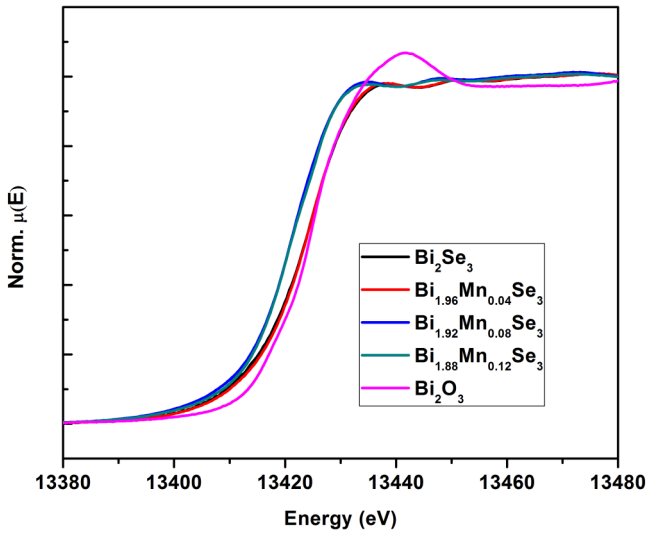


FIG. 8. Normalized XANES spectra of undoped $Bi_2Se_3$ and Mn doped $Bi_2Se_3$ crystals along with that of $Bi_2O_3$ powder at Bi L3 edge.

The qualitative information about the local structure have been obtained by converting the oscillations in the absorption spectra $\mu(E)$ to absorption function $\chi(E)$ defined as follows:

$$\chi(E) = \frac{\mu(E) - \mu_0(E)}{\Delta\mu_0(E_0)}, \tag{2}$$

where $E_0$ is absorption edge energy, $\mu_0(E)$ is the bare atom background and $\Delta\mu_0(E_0)$ is the step in $\mu(E)$ value at the absorption edge. The energy dependent absorption coefficient $\chi(E)$ has been converted to the wave number dependent absorption coefficient $\chi(k)$ using the relation

$$K = \sqrt{\frac{2m(E - E_0)}{\hbar^2}}, \tag{3}$$

where m is the electron mass. $\chi(k)$ is weighted by $k^2$ to amplify the oscillation at high $k$ and the $\chi(k)k^2$ functions are subsequently Fourier transformed in $R$ space to generate the $\chi(R)$ versus $R$ plots in terms of the real distances from the center of the absorbing atom. The ATHENA subroutine available within the DEMETER [44] software package has been used for the above data reduction. For the present set of samples, $k$ windows of 3–12 $Å^{-1}$, 3–9.5 $Å^{-1}$ and 3–9 $Å^{-1}$ have been used for Bi $L_3$ edge, Se K edge and Mn K edge data, respectively.

In Fig. 10 the main peak around 2.34 Å has contribution from Bi-Se coordination shells. The intensity of this peak decreases slightly with an increase in Mn doping since doping of Mn atom in $Bi_2Se_3$ increases the disorder in Bi-Se coordination shell. Also there is slight increase in Bi-Se bond length with Mn doping which is as expected since ionic radius of $Mn^{+2}$ being smaller (0.87 Å) than that of $Bi^{+3}$ (1.03 Å) contracts the lattice at Mn sites and allows Bi sites to expand. To have a quantitative estimation we have fitted the experimental $\chi(r)$ versus $r$ plots with the theoretically generated data. Theoretical $\chi(R)$ versus $R$ plots have been generated using the standard EXAFS equation [45] and using the basic crystallographic information of $Bi_2Se_3$ crystal structure [46]. The coordination shells generated from $Bi_2Se_3$ crystal structure which are used for EXAFS data fitting are shown in Fig. 9.

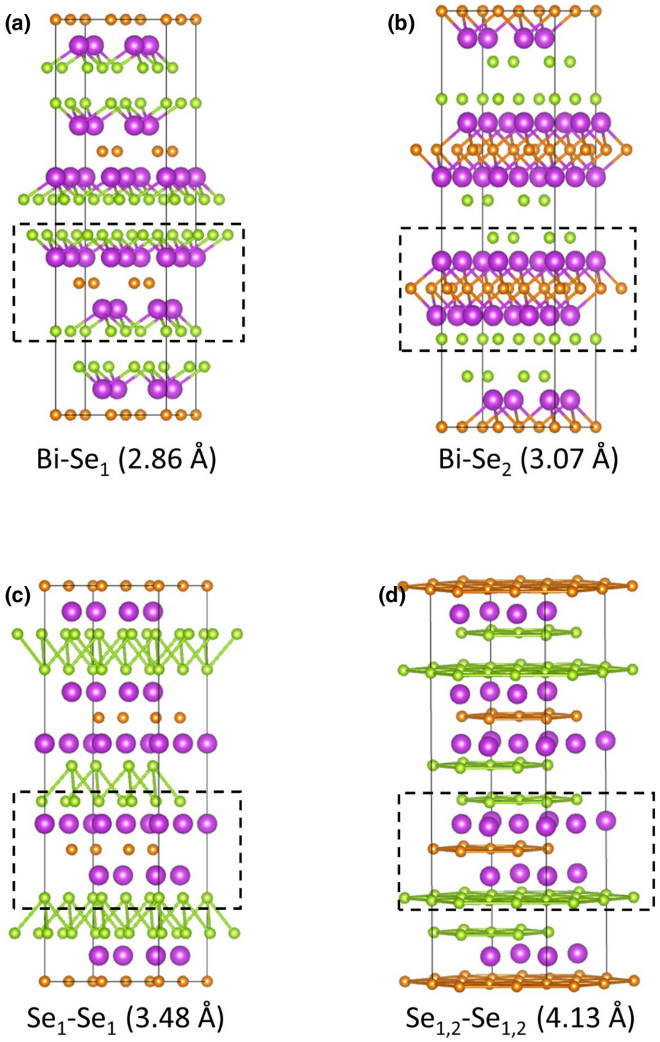


FIG. 9. The different coordination shells generated from $Bi_2Se_3$ crystal structure which are used in EXAFS fitting at Bi $L_3$ and Se K edge, (a) Bi-$Se_1$, (b) Bi-$Se_2$, (c) $Se_1$-$Se_1$, and (d) $Se_{1,2}$-$Se_{1,2}$.

During fitting, bond distances ($R$) and coordination numbers ($N$) have been used as fitting parameters. The goodness of fit has been determined by the value of the $R_{\text{factor}}$ defined by

$$R_{\text{factor}} = \Sigma \frac{[\text{Im}(\chi_{\text{dat}}(r_i) - \chi_{th}(r_i)]^2 + [\text{Re}(\chi_{\text{dat}}(r_i) - \chi_{th}(r_i)]^2}{[\text{Im}(\chi_{\text{dat}}(r_i)]^2 + [\text{Re}(\chi_{\text{dat}}(r_i)]^2}, \tag{4}$$

where $\chi_{\text{dat}}$ and $\chi_{th}$ refer to the experimental and theoretical $\chi(r)$ values respectively and Im and Re refer to the imaginary and real parts of the respective quantities. The fitting has been donein the range of 1.7 Å–3.0 Å and the best fit values of the parameters have been obtained. The subroutines ATOMS and ARTEMIS available within the DEMETER software package [44] have been used for generation of the theoretical paths from the crystallographic structure and fitting of the experimental data with the theoretical simulation. The best fit theoretical plots have been shown in Fig. 10 along with the experimental

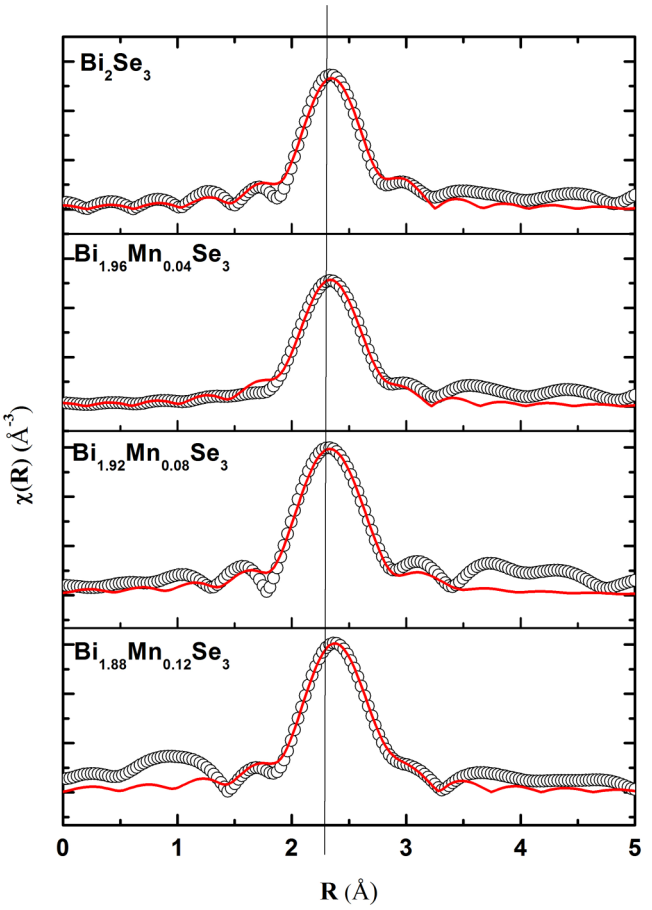


FIG. 10. Fourier transformed EXAFS spectra of undoped and Mn doped $Bi_2Se_3$ crystals measured at Bi L3 edge. The experimental data are represented by scatter points and theoretical fits are represented by solid lines.

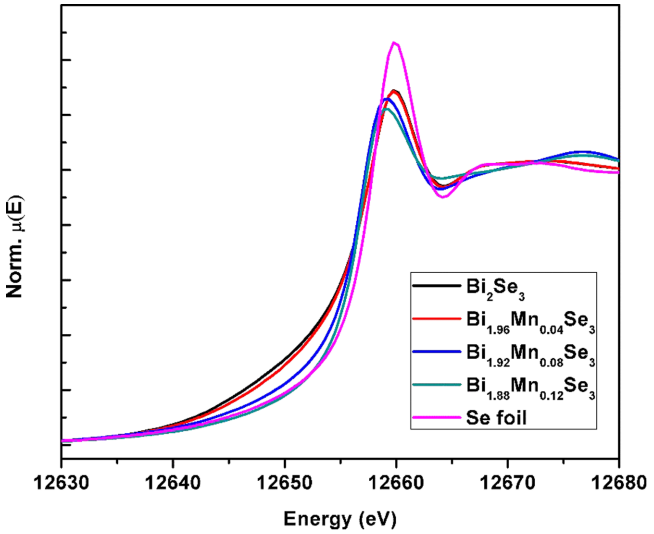


FIG. 11. XANES spectra of undoped and Mn doped $Bi_2Se_3$ crystal at Se $K$ edge along with that of Se foil.

data and the best fit parameters are shown in Table III. It can be seen that there is an increase in the Debye-Waller factor, which represents disorder in the system with Mn doping concentration. However, we could not detect any systematic change in the Bi-Se bond lengths since the change might be within the error bars of the EXAFS data. It should be mentioned here that according to the theoretical calculations also, the Bi-Se bond distances do not change much with Mn doping. The Bi-Se bond lengths in pristine $Bi_2Se_3$ are 2.86 Å and 3.07 Å (as shown in Fig. 9). In the Mn doped system, it has been observed from the DFT-relaxed structure that the Bi-Se1 bond length in the first Se coordination shells of Bi atoms near Mn atoms split into three values (2.862, 2.849, and 2.889 Å), the average bond length remaining at 2.86 Å. Since this only happens near the dopant sites and Mn doping concentration is very low in the $Bi_2Se_3$ system, it may not reflect in the EXAFS data which has an error bar of ±0.01 Å.

XANES spectra of the samples measured at Se K edge are shown in Fig. 11 along with that of a standard Se foil. Se absorption edge of the film is found to lie at lower energy compared to that of the Se foil in conformity with the fact that Se ions are present in the film in -2 oxidation state. It has also been observed that with increase in Mn doping, Se K edge continuously shifts to higher energy in corroboration with the fact that with Mn doping Bi $L_3$ edge shifts to lower energy.

Figure 12 shows the experimental Fourier transformed EXAFS spectra ($\chi(R)$ versus $R$ plots) of Mn doped $Bi_2Se_3$ samples measured at Se K edge along with the best fit theoretical plots. The EXAFS data have been fitted in $R$ range of 1.8 Å – 4.2 Å. The peak maxima at 2.18 and 2.81 Å have contributions from Se – Bi coordination shells. The peak maxima at 3.91 Å have contributions from Se – Se coordination shells. The best fit parameters are shown in Table IV. It can be found from Tables III and IV that all the parameters

TABLE III. Best fit EXAFS parameters of Mn doped $Bi_2Se_3$ crystal at Bi $L_3$ edge (the parameters in the parenthesis are the theoretical values as per the structure).

| Path | Parameter | $Bi_2Se_3$ | $Bi_{1.96}Mn_{0.04}Se_3$ | $Bi_{1.92}Mn_{0.08}Se_3$ | $Bi_{1.88}Mn_{0.12}Se_3$ |
|---|---|---|---|---|---|
| **Bi−Se$_1$** | R (Å) (2.86) | 2.82 ± 0.01 | 2.80 ± 0.01 | 2.84 ± 0.01 | 2.81 ± 0.01 |
| | N (3) | 3.0 ± 0.09 | 3.0 ± 0.06 | 3.0 ± 0.09 | 3.0 ± 0.06 |
| | $\sigma^2$ | 0.008 ± 0.0002 | 0.0088 ± 0.0002 | 0.0039 ± 0.0001 | 0.0092 ± 0.0001 |
| **Bi−Se$_2$** | R (Å) (3.07) | 3.04 ± 0.01 | 3.03 ± 0.01 | 3.03 ± 0.01 | 3.05 ± 0.01 |
| | N (3) | 3.0 ± 0.09 | 3.0 ± 0.06 | 3.0 ± 0.09 | 3.0 ± 0.06 |
| | $\sigma^2$ | 0.014 ± 0.0007 | 0.017 ± 0.0007 | 0.013 ± 0.0007 | 0.015 ± 0.0004 |
| | $R_{factor}$ | 0.012 | 0.006 | 0.01 | 0.003 |

TABLE IV. Best fit EXAFS parameter of Mn doped $Bi_2Se_3$ crystal at Se *K* edge (the parameters in the parenthesis are the theoretical values as per the structure).

| Path | Parameter | $Bi_2Se_3$ | $Bi_{1.96}Mn_{0.04}Se_3$ | $Bi_{1.92}Mn_{0.08}Se_3$ | $Bi_{1.88}Mn_{0.12}Se_3$ |
|---|---|---|---|---|---|
| **$Se_1$−Bi** | R (Å) (2.86) | 2.88 ± 0.01 | 2.88 ± 0.01 | 2.87 ± 0.01 | 2.89 ± 0.01 |
| | N (3) | 3.0 ± 0.03 | 3.0 ± 0.03 | 3.0 ± 0.03 | 3.0 ± 0.03 |
| | $\sigma^2$ | 0.0078 ± 0.0001 | 0.0072 ± 0.0001 | 0.0097 ± 0.0002 | 0.0107 ± 0.0002 |
| **$Se_2$−Bi** | R (Å) (3.07) | 3.04 ± 0.01 | 3.05 ± 0.01 | 3.07 ± 0.01 | 3.12 ± 0.01 |
| | N (6) | 6.0 ± 0.06 | 6.0 ± 0.06 | 6.0 ± 0.05 | 6.0 ± 0.06 |
| | $\sigma^2$ | 0.016 ± 0.0002 | 0.015 ± 0.0001 | 0.021 ± 0.0002 | 0.018 ± 0.0002 |
| **$Se_1$−$Se_1$** | R (Å) (3.48) | 3.39 ± 0.02 | 3.38 ± 0.02 | 3.36 ± 0.01 | 3.26 ± 0.01 |
| | N (3) | 3.0 ± 0.03 | 3.0 ± 0.03 | 3.0 ± 0.03 | 3.0 ± 0.03 |
| | $\sigma^2$ | 0.04 ± 0.004 | 0.04 ± 0.003 | 0.027 ± 0.001 | 0.037 ± 0.002 |
| **$Se_{1,2}$−$Se_{1,2}$** | R (Å) (4.13) | 4.13 ± 0.01 | 4.14 ± 0.01 | 4.13 ± 0.01 | 4.10 ± 0.026 |
| | N (6) | 6.0 ± 0.06 | 6.0 ± 0.06 | 6.0 ± 0.06 | 6.0 ± 0.06 |
| | $\sigma^2$ | 0.028 ± 0.001 | 0.028 ± 0.0005 | 0.025 ± 0.0004 | 0.028 ± 0.0005 |
| | $R_{factor}$ | 0.006 | 0.003 | 0.003 | 0.015 |

are fitted reasonably well with the $Bi_2Se_3$ crystal structure. From Fig. 12 and Table IV, it is evident that the Se sublattice remains unperturbed due to Mn doping, manifesting the fact that Mn atoms are being substituted at Bi sites and not at Se sites. This corroborates our earlier findings from DFT based *ab initio* theoretical calculations that transition metal doping at Se sites leads to significant increase in formation energy [18] and hence is less probable.

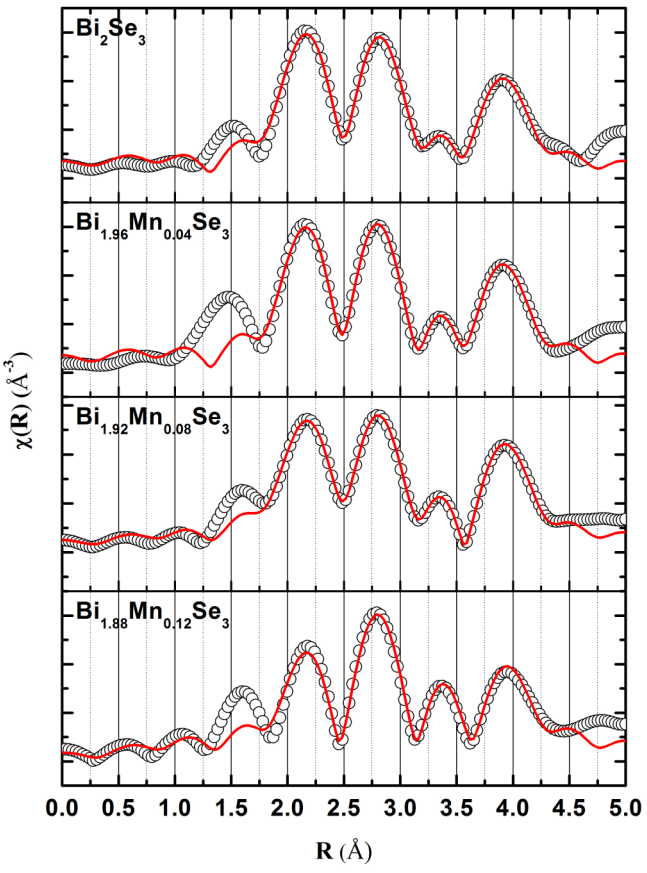


FIG. 12. Fourier transformed EXAFS spectra of Mn doped $Bi_2Se_3$ crystals measured at Se K edge along with best fit theoretical simulations. The experimental spectra are represented by scatter points and theoretical fits are represented by solid lines.

The van der Waals gap distance can be guessed qualitatively through $Se_1$-$Se_1$ bond length shown in Fig. 9. This coordination shell is made of Se atoms along the van der Waal band gap and the $Se_1$-$Se_1$ bond length is 3.48 Å and at an angle of 43.0691 ° with *c* lattice axis. Thus $Se_1$-$Se_1$ bond length will not change much if we have decreased lattice axis 'a' and increased lattice axis *c*. This is the case of 2% and 4% Mn doped $Bi_2Se_3$, as it was suggested by DFT calculations and EXAFS fitting. When the both lattice axis a and *c* decreases (6% Mn doping case), we will certainly have shorter $Se_1$-$Se_1$ bond length. We have indeed obtained a shorter $Se_1$-$Se_1$ bond length for 6% Mn doped $Bi_2Se_3$ in EXAFS fitting as shown in Table IV. Thus the above results show that our theoretical findings from DFT and experimental findings from EXAFS corroborate each other.

The XAS data for Mn doped $Bi_2Se_3$ were recorded in the fluorescence mode at Mn K edge. The XANES data of all the samples along with Mn standards are shown in Fig. 13. It shows that the absorption edges of Mn doped $Bi_2Se_3$ samples lie between Mn absorption edges of Mn metal and $MnO_2$. The XANES data exclude the possibility of the formation of a Mn cluster or oxide in the doped samples. Figure 14 shows the Fourier transformed EXAFS spectra or ($\chi(R)$ versus $R$) plot of Mn doped $Bi_2Se_3$ measured at Mn K edge along with the best fit theoretical simulations. The EXAFS data has been fitted in the range of 1.7 Å–3.0 Å by taking the optimized Mn doped $Bi_2Se_3$ structure, obtained through *ab initio* DFT calculations discussed above. The best fit parameters are shown in Table V. It shows that during doping Mn atoms replace Bi atoms as suggested by DFT calculations. It can be seen from Fig. 14 that the FT-EXAFS spectra at Bi and Mn edges are almost similar in nature manifesting that Mn atoms are indeed substituted at Bi sites. From Tables III and V it can be seen that Mn-Se bond lengths are less than the Bi-Se bond lengths which is due to smaller ionic radii of Mn compared to Bi. It

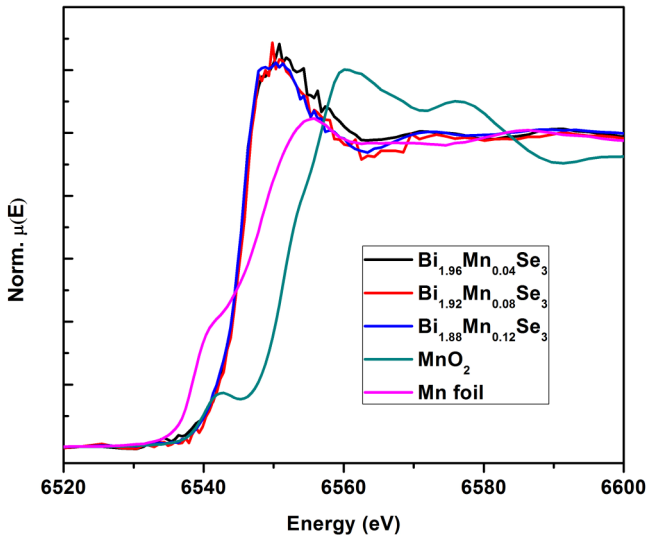


FIG. 13. Normalized XANES spectra of Mn doped $Bi_2Se_3$ crystal along with $MnO_2$ and Mn foil at Mn K edge.

should be mentioned here that EXAFS data for the 2% Mn doped sample could not be analyzed due to poor quality of the data.

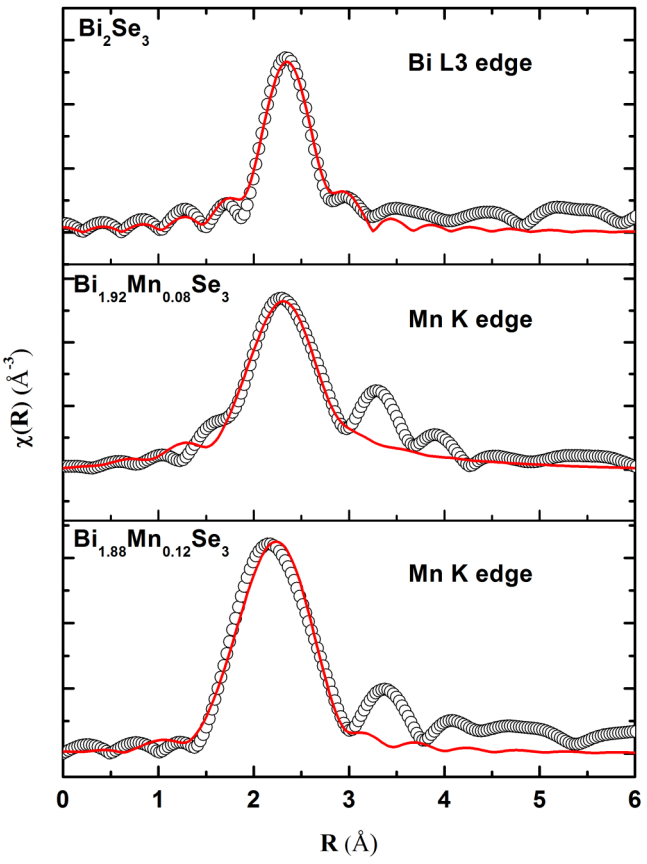


FIG. 14. Fourier transformed EXAFS spectra of Mn doped $Bi_2Se_3$ crystal at Mn K edge along with $Bi_2Se_3$ crystal data at Bi L3 edge (top panel). The experimental spectra are represented by scatter points and theoretical fits are represented by solid lines.

TABLE V. Best fit EXAFS parameter of Mn doped $Bi_2Se_3$ cystal at the Mn K edge (the parameters in the parenthesis are the theoretical values as per the structure).

| Path | Parameter | $Bi_{1.92}Mn_{0.08}Se_3$ | Parameter | $Bi_{1.88}Mn_{0.12}Se_3$ |
|---|---|---|---|---|
| **Mn−Se$_1$** | R (Å) (2.59) | $2.54 \pm 0.01$ | R (Å) (2.56) | $2.56 \pm 0.01$ |
| | N (3) | $3.0 \pm 0.12$ | N (3) | $3.0 \pm 0.21$ |
| | $\sigma^2$ | $0.016 \pm 0.00$ | $\sigma^2$ | 0.001 |
| **Mn−Se$_2$** | R (Å) (2.65) | $2.66 \pm 0.01$ | R (Å) (2.70) | $2.70 \pm 0.01$ |
| | N (3) | $3.0 \pm 0.12$ | N (3) | $3.0 \pm 0.21$ |
| | $\sigma^2$ | 0.001 | $\sigma^2$ | 0.001 |
| | $R_{factor}$ | 0.009 | $R_{factor}$ | 0.02 |

## V. CONCLUSIONS

Mn doped $Bi_2Se_3$ systems have been investigated both theoretically and experimentally. *Ab initio* DFT based theoretical calculations shows that with Mn doping the lattice constant a of $Bi_2Se_3$ decreases while the lattice constant *c* initially decreases, however, it increases again at higher Mn doping concentration which is due to the presence of two competing phenomena: reduction in QL size and increase in van der Waal gap due to Mn doping. The band structure calculations show band inversion near the top of conduction band and bottom of valence band and gapless surface states which are characteristics of topological insulators and also reduction in band gap upon Mn doping. The above results have been corroborated by direct ARPES measurements using synchrotron radiation on undoped and Mn doped $Bi_2Se_3$ single crystals grown by the Bridgman technique. The ARPES data shows clear band gap in the undoped samples, gap less surface states and reduction in band gap on Mn doping corroborating with the theoretical results. ARPES data also shows opening of gap in surface states near Fermi level in Mn doped sample which is very important for application of TI systems in various spintronic applications and also to realize various exotic physical phenomena. Further, substitutional doping of Mn at Bi sites has been investigated by XANES and EXAFS measurements using synchrotron radiation. XANES data shows that Bi $L_3$ edge lies at higher energy and Se K edge lies at lower energies than their respective metallic counterparts ascertaining formation of $Bi_2Se_3$ compound. However, with Mn doping the Bi $L_3$ edge shifts to lower energy since Bi sites become less positive upon Mn inclusion in the lattice and to compensate this Se K edge also shifts to higher energy. The increase in Debye-Waller (disorder) factor with Mn doping in Bi $L_3$ edge EXAFS data and also the fact that with Mn K edge FT-EXAFS pattern resembles that of Bi L3 edge FT-EXAFS pattern ascertain that Mn ions substitute at Bi sites in the $Bi_2Se_3$ lattice as predicted from formation energy calculations by DFT.

## ACKNOWLEDGMENTS

S. Paul of RRCAT is thanked for experimental support in ARPES measurements and Dr. D. Karmakar of BARC is acknowledged for her support in DFT calculations. The crystal structures in Figs. 1 and 9 were visualized with the VESTA [47] software. This work has been carried out using

internal funding of our organisation (Bhabha Atomic research Centre) and has not been supported by any external funding. The information provided for funding is correct and complete.

[1] B. A. Bernevig and S.-C. Zhang, Phys. Rev. Lett. **96**, 106802 (2006).
[2] L. Fu, C. L. Kane, and E. J. Mele, Phys. Rev. Lett. **98**, 106803 (2007).
[3] H. Zhang, C.-X. Liu, X.-L. Qi, X. Dai, Z. Fang, and S.-C. Zhang, Nat. Phys. **5**, 438 (2009).
[4] Y. Xia, D. Qian, D. Hsieh, L. Wray, A. Pal, H. Lin, A. Bansil, D. Grauer, Y. S. Hor, R. J. Cava *et al.*, Nat. Phys. **5**, 398 (2009).
[5] D. Hsieh, Y. Xia, D. Qian, L. Wray, J. H. Dil, F. Meier, J. Osterwalder, L. Patthey, J. G. Checkelsky, N. P. Ong *et al.*, Nature (London) **460**, 1101 (2009).
[6] M. Z. Hasan and C. L. Kane, Rev. Mod. Phys. **82**, 3045 (2010).
[7] D. Pesin and A. H. MacDonald, Nat. Mater. **11**, 409 (2012).
[8] C. Nayak, S. H. Simon, A. Stern, M. Freedman, and S. Das Sarma, Rev. Mod. Phys. **80**, 1083 (2008).
[9] A. Y. Kitaev, Ann. Phys. **303**, 2 (2003).
[10] Q. Liu, C.-X. Liu, C. Xu, X.-L. Qi, and S.-C. Zhang, Phys. Rev. Lett. **102**, 156603 (2009).
[11] L. Andrew Wray, S.-Yang Xu, Y. Xia, D. Hsieh, A. V. Fedorov, Y. San Hor, R. J. Cava, A. Bansil, H. Lin, and M. Zahid Hasan, Nat. Phys. **7**, 32 (2011).
[12] X.-L. Qi, T. L. Hughes, and S.-C. Zhang, Phys. Rev. B **78**, 195424 (2008).
[13] C.-Z. Chang, J. Zhang, X. Feng, J. Shen, Z. Zhang, M. Guo, K. Li, Y. Ou, P. Wei, L.-L. Wang *et al.*, Science **340**, 167 (2013).
[14] X.-L. Qi, R. Li, J. Zang, and S.-C. Zhang, Science **323**, 1184 (2009).
[15] S.-Q. Shen, in *Topological Insulators* (Springer, Berlin, 2017), p. 189.
[16] Y. L. Chen, J.-H. Chu, J. G. Analytis, Z. K. Liu, K. Igarashi, H.-H. Kuo, X. L. Qi, S. K. Mo, R. G. Moore, D. H. Lu *et al.*, Science **329**, 659 (2010).
[17] S.-Y. Xu, M. Neupane, C. Liu, D. Zhang, A. Richardella, L. Andrew Wray, N. Alidoust, M. Leandersson, Thiagarajan Balasubramanian, Jaime Sánchez-Barriga *et al.*, Nat. Phys. **8**, 616 (2012).
[18] R. Kumar and D. Bhattacharyya, Superlattices Microstruct. **159**, 107033 (2021).
[19] J. Sánchez-Barriga, A. Varykhalov, G. Springholz, H. Steiner, R. Kirchschlager, G. Bauer, O. Caha, E. Schierle, E. Weschke, and A. A. Unal, Nat. Commun. **7**, 10559 (2016).
[20] G. Kresse and J. Hafner, Phys. Rev. B **47**, 558 (1993).
[21] G. Kresse and J. Hafner, Phys. Rev. B **49**, 14251 (1994).
[22] G. Kresse and J. Furthmüller, Phys. Rev. B **54**, 11169 (1996).
[23] G. Kresse and J. Furthmüller, Comput. Mater. Sci. **6**, 15 (1996).
[24] P. E. Blöchl, O. Jepsen, and O. K. Andersen, Phys. Rev. B **49**, 16223 (1994).
[25] G. Kresse and D. Joubert, Phys. Rev. B **59**, 1758 (1999).
[26] J. P. Perdew, K. Burke, and M. Ernzerhof, Phys. Rev. Lett. **77**, 3865 (1996).
[27] S. Grimme, J. Comput. Chem. **27**, 1787 (2006).
[28] https://www.rrcat.gov.in/technology/accel/srul/beamlines/arpes.html.
[29] S. Basu, C. Nayak, A. Yadav, A. Agrawal, A. Poswal, D. Bhattacharyya, S. Jha, and N. Sahoo, in *Journal of Physics: Conference Series* (IOP Publishing, New York, 2014), p. 012032.
[30] A. K. Poswal, A. Agrawal, A. K. Yadav, C. Nayak, S. Basu, S. R. Kane, C. K. Garg, D. Bhattachryya, S. N. Jha, and N. K. Sahoo, in *AIP Conference Proceedings 1591* (American Institute of Physics, Melville, NY, 2014), p. 649.
[31] J. Wiese and L. Muldawer, J. Phys. Chem. Solids **15**, 13 (1960).
[32] W. Cheng and S.-F. Ren, Phys. Rev. B **83**, 094301 (2011).
[33] S. B. Zhang and J. E. Northrup, Phys. Rev. Lett. **67**, 2339 (1991).
[34] J.-M. Zhang, W. Ming, Z. Huang, G.-B. Liu, X. Kou, Y. Fan, K. L. Wang, and Y. Yao, Phys. Rev. B **88**, 235131 (2013).
[35] L. B. Abdalla, L. Seixas, T. M. Schmidt, R. H. Miwa, and A. Fazzio, Phys. Rev. B **88**, 045312 (2013).
[36] J.-M. Zhang, W. Zhu, Y. Zhang, D. Xiao, and Y. Yao, Phys. Rev. Lett. **109**, 266405 (2012).
[37] Z.-H. Pan, E. Vescovo, A. V. Fedorov, D. Gardner, Y. S. Lee, S. Chu, G. D. Gu, and T. Valla, Phys. Rev. Lett. **106**, 257004 (2011).
[38] I. A. Nechaev, R. C. Hatch, M. Bianchi, D. Guan, C. Friedrich, I. Aguilera, J. L. Mi, B. B. Iversen, S. Blügel, P. Hofmann *et al.*, Phys. Rev. B **87**, 121111(R) (2013).
[39] S. Kim, M. Ye, K. Kuroda, Y. Yamada, E. E. Krasovskii, E. V. Chulkov, K. Miyamoto, M. Nakatake, T. Okuda, Y. Ueda *et al.*, Phys. Rev. Lett. **107**, 056803 (2011).
[40] M. Bianchi, D. Guan, S. Bao, J. Mi, B. B. Iversen, P. D. C. King, and P. Hofmann, Nat. Commun. **1**, 128 (2010).
[41] D. Biswas and K. Maiti, J. Electron Spectrosc. Relat. Phenom. **208**, 90 (2016).
[42] A. L. Allred, J. Inorg. Nucl. Chem. **17**, 215 (1961).
[43] J. E. Huheey, E. A. Keiter, R. L. Keiter, and O. K. Medhi, *Inorganic Chemistry: Principles of Structure and Reactivity* (Pearson Education, India, 2006).
[44] M. Newville, B. Ravel, D. Haskel, J. J. Rehr, E. A. Stern, and Y. Yacoby, Physica B: Cond. Matter **208-209**, 154 (1995).
[45] M. Newville, J. Synchrotron Radiat. **8**, 96 (2001).
[46] S. Nakajima, J. Phys. Chem. Solids **24**, 479 (1963).
[47] K. Momma and F. Izumi, J. Appl. Crystallogr. **44**, 1272 (2011).